CHAPTER 5

A study on Al^{3+} ion storage in hydrated vanadate and aluminium doped hydrated vanadate

A study on Al^{3+} ion storage in hydrated vanadate and aluminium doped hydrated vanadate

5.1 Introduction

Recently, vanadium oxide based materials have garnered considerable attention due to their properties such as metal to insulator transition, multiple oxidation states (from +2 to +5), thereby able to transfer multi electrons, distinctive layered structure, unique physical and chemical properties [1-3]. These materials can be used as catalysts [4, 5], gas sensors [6] and electrode materials for batteries [7, 8] and supercapacitor [1-3]. But in aqueous electrolyte based energy storage, vanadium based materials encounter the problems such structural collapse and dissolution during charge-discharge process. However, these drawbacks can be overcome by expanding the interlayer spacing of hydrated vanadium with guest ions, and use of gel electrolytes [9]. Lee et al. were the first who prepared hydrated vanadium ($V_2O_5.nH_2O$) and utilized for supercapacitor application in KCl based aqueous electrolyte [10]. Fan et al. demonstrated hydrated vanadium ($V_2O_5.nH_2O$)/reduced graphene oxide (rGO) composites with extended interlayer spacing and applied for NH_4^+ ion storage, exhibiting a specific capacitance about 600 Fg^{-1} at current density (=0.2 Ag^{-1}) with 93 % capacity retention over 10000 cycles in PVA/NH_4Cl gel electrolyte [11]. Jing et al. inserted Al^{3+} in hydrated vanadium and prepared $Al_{0.34}V_2O_{12}.2.4H_2O$ (AlVOH) for aqueous zinc ion batteries, which exhibited a specific capacity ~ 176 $mAhg^{-1}$ at current density of 20 Ag^{-1} after 2000 discharge cycles [12]. Du et al. pre intercalated Mg^{2+} ion in hydrated vanadium and utilized for zinc ion batteries, achieving a specific capacity of 386 $mAhg^{-1}$ at a current density of 0.1 Ag^{-1}, and a capacity retention of 91 % after 1500 discharge cycles at current density of 5 Ag^{-1} [13]. Depending on these findings, we embarked an extensive investigation of Al^{3+} ion storage in hydrated vanadium or hydrated vanadate. Therefore, this chapter focuses on evaluating the electrochemical storage capacity of Al^{3+} ion in hydrated vanadate and aluminum doped hydrated vanadate, both in aqueous and gel electrolytes.

5.2 Experimental Section

5.2.1 Materials

Vanadium pentaoxide (V_2O_5, Lobachemie Pvt. Ltd.), Hydrogen peroxide 30 % (H_2O_2), Aluminuim sulphate 16-hydrate, Aluminium chloride anhydrous powder and Aluminium nitrate monohydrate were collected from (Merck), Polyethylene oxide and Polyvinylidene fluoride (PVDF) (from Sigma Aldrich), Carbon black and N-methyl-2-pyrrolidone (from Alfa aesar). Ethanol and Distilled water.

5.2.2 Synthesis

Hydrated vanadate (abbreviated as VOH) was synthesized using a known hydrothermal procedure, as reported in the literature [14]. In a brief, 0.364 g of V_2O_5 was dissolved in a solution containing 2 ml of H_2O_2 and 80 ml of Millipore water. Thereafter, the mixture was transferred to a 100 ml stainless steel autoclave and heated at 120 ^oC for 6 h. Then, after cooling down to room temperature, the dark red precipitate was filtered and washed with water and ethanol for several times and dried overnight in an electric oven at 70 ^oC. Finally, the product was further dried at 120 ^oC for 5 h. Again, aluminium doped hydrated vanadate (AlVOH) using the similar process of VOH, with the addition of 0.171 g of $Al_2(SO_4)_3.16H_2O$ in the above solution.

5.2.3 Characterization

The physicochemical properties of the prepared material were investigated by X ray diffraction (BRUER AXS D8 FOCUS, Cu-K_a radiation; λ=1.5406 Å) and ultra high resolution FESEM (JSM-7200F), Raman spectroscopy (RENISHAW BASIS SERIES WITH 515 LASER, RENISHAW, UK) and Fourier Transform Infrared Spectrometer (FTIR, SPECTRUM 100 and FORNTIER IR, Perkin Elmer).

5.2.4 Electrochemical Analysis

Then a homogeneous slurry was prepared by merging the active material, carbon black and polyvinylidene fluoride (PVDF) in weight ratio of 8:1:1 using N-methyl-2 pyrrolidone (NMP) as the solvent. Then it was drop coated on graphite paper and dried at 90 ^oC overnight. The mass on the electrodes were recorded as (1-1.5) mg. The electrochemical experiments were conducted in Metrohm Autolab

(PGSTAT302N) where VOH, Ag/AgCl and platinum were employed as working electrode, reference electrode and counter electrode respectively. Aqueous $AlCl_3$, $Al_2(SO_4)_3$, $Al(NO_3)_3$ and $AlCl_3$/PEO gel electrolytes were used throughout the experiments.

5.3 Results and discussion

Figure 5.1a shows the XRD spectra of VOH, where all the diffraction peaks are indexed according to the PDF No: 40-1296, confirming the monoclinic structure with space group C2/m. Figure 5.1b presents the Raman analysis of VOH, with Raman peaks centered at 142 cm^{-1}, 282 cm^{-1} and 402 cm^{-1} corresponding to the bending vibrations of O-V-O, V^{5+}=O and V-O-V respectively [14-16]. Similarly, the stretching vibrations of V-O, V^{5+}=O and V-O-V could be recognized at 523 cm^{-1}, 991 cm^{-1} and 702 cm^{-1} respectively [14-16]. The FT-IR spectra of VOH is shown in (Figure 5.1c). The absorptions at 518 cm^{-1} and 756 cm^{-1} were attributed to the symmetric and asymmetric vibration of V-O-V bonds respectively, while the absorption at 1011 cm^{-1} corresponds to the V=O stretching vibration [14-16]. Moreover, the absorptions at 1626 cm^{-1} and 3420 cm^{-1} were ascribed to the bending and stretching vibrations of H-O bonds from water molecules [14-17].

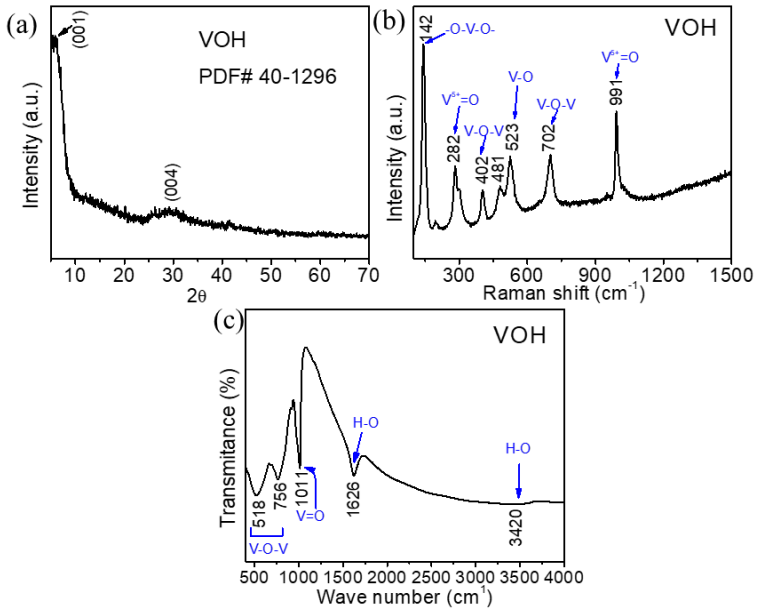

Figure 5.1: (a) XRD pattern, (b) Raman -spectrum and (c) FTIR spectrum of VOH.

The surface morphology as shown in (Figure 5.2 (a-b)) reveals the formation of nanorod structure having the diameter ranging from 0.2 μm to 0.3 μm and length ~ 2 μm.

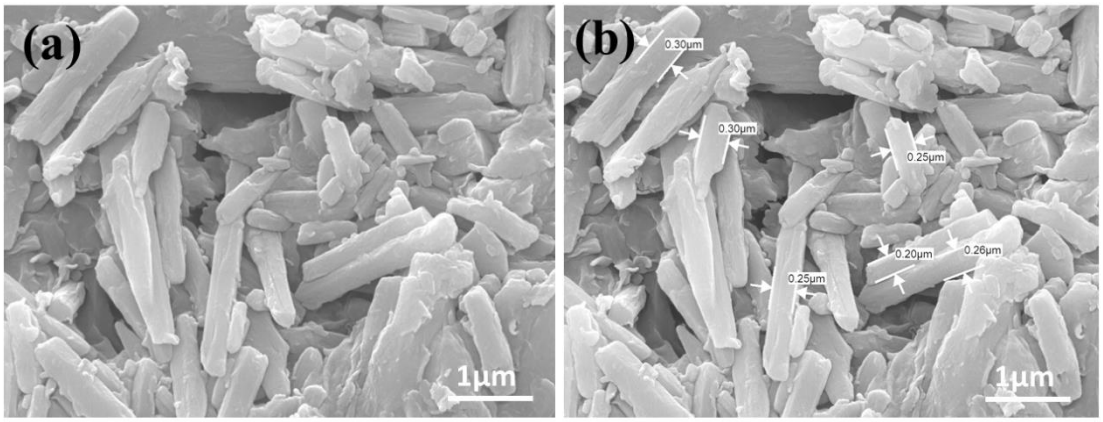

Figure 5.2: (a-b) FESEM images of VOH.

Now, in order to investigate the electrochemical activity of VOH, at first Cyclic Voltammetry (CV) experiments were conducted in $AlCl_3$ aqueous electrolytes at different concentrations of 0.25 M, 0.5 M and 1 M over the potential range of -0.7 V to 0.7 V (vs Ag/AgCl) at scan rate of 2 mVs^{-1}. As shown in Figure 5.3a, the CV profile for 0.25 M $AlCl_3$, exhibits two pairs of redox peaks: a prominent redox peak at 0.07 V/0.32 V and a smaller hump at -0.29 V/-0.14 V, referred to as A/A$^{/}$ and B/B$^{/}$, respectively. Similar CV profiles were also observed for 0.5 M and 1 M $AlCl_3$ electrolytes (Figure 5.3b and 5.3c). However, the current response and area covered by the CV curve is greater in the case of 1 M $AlCl_3$ (Figure 5.3d), indicating higher specific capacitance due to the large number of ions participating at the electrode/electrolyte interface.

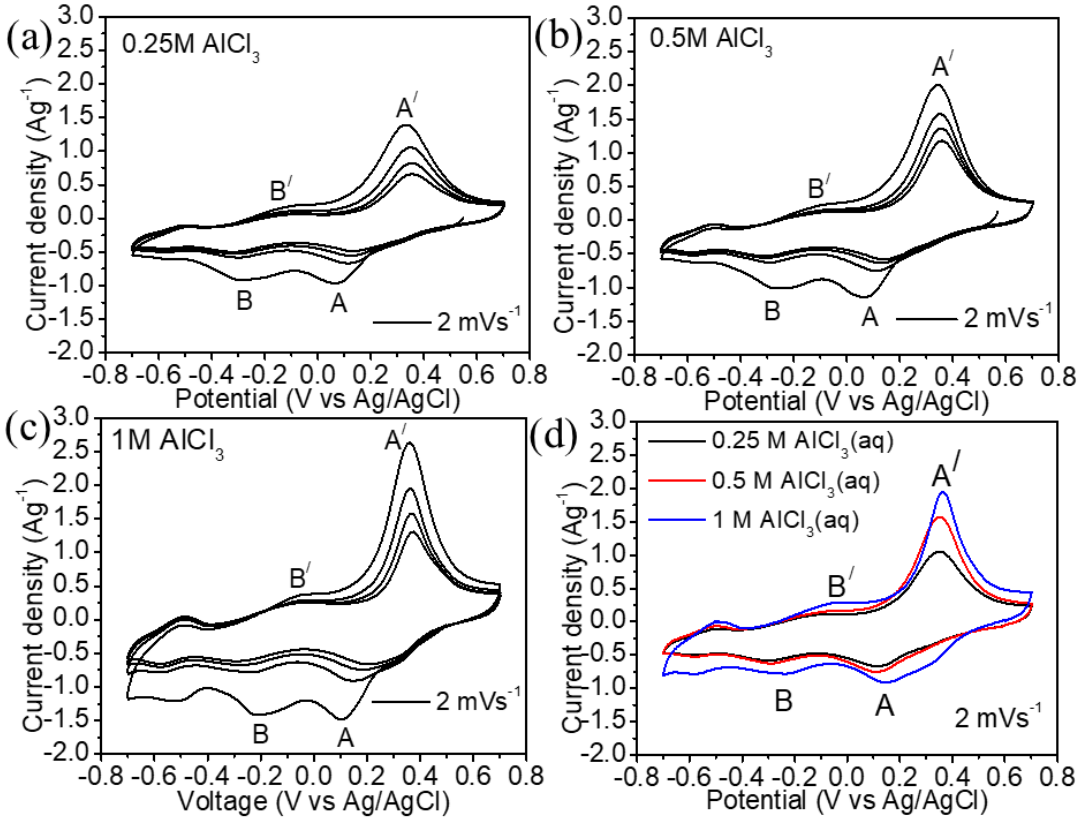

Figure 5.3: CV profiles of VOH in (a) 0.25 M $AlCl_3$, (b) 0.5 M $AlCl_3$ and (c) 1 M $AlCl_3$ aqueous electrolytes and (d) the comparison of area under the curves.

CV experiments were also conducted using 0.5 M $Al_2(SO_4)_3$ and 1 M $Al(NO_3)$ aqueous electrolytes under the identical potential range (vs. Ag/AgCl) and scan rates. Figure 5.4a shows the CV profile of VOH in 0.5 M $Al_2(SO_4)_3$ electrolyte with redox peaks centered at 0.08 V/0.44 V and -0.22 V/0.02 V, labeled as C/C$^{/}$ and D/D$^{/}$ respectively. In contrast, the CV profile for 1 M $Al(NO_3)_3$ reveals a sharp decrease in current at the lower potential side (Figure 5.4b). However, the redox peaks noticed at 0.13 V/0.38 V and -0.14 V/ -0.02 V, are designated as E/E$^{/}$ and F/F$^{/}$ respectively (Figure 5.4b).

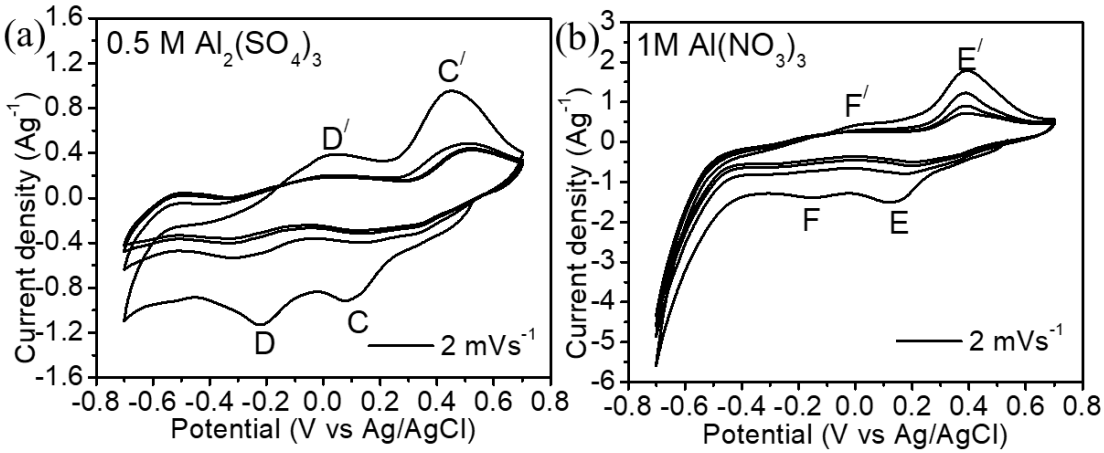

Figure 5.4: CV profiles of VOH in (a) 0.M M $Al_2(SO_4)_3$ and (b) 1 M $Al(NO_3)_3$ aqueous electrolytes.

Besides, CV experiment was carried out using 1 M $AlCl_3$/PEO gel electrolyte (Figure 5.5). In this case, the prominent redox peak was noticed at 0.14 V/0.44 V along with smaller humps at -0.18 V/-0.03 V. These peaks are abbreviated as G/G$^{/}$ and H/H$^{/}$ respectively. However, the CV curves for gel electrolyte appear more overlapping compared to those for aqueous electrolyte (Figure 5.5 and 5.3), indicating better electrochemical stability in the gel electrolyte.

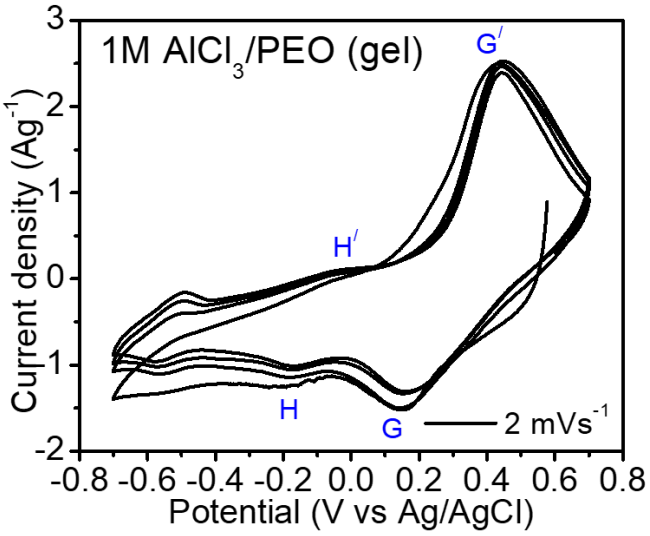

Figure 5.5: CV profile of VOH in 1 M $AlCl_3$/PEO (gel) electrolyte.

Now, CV experiments were performed with VOH in 1 M LiCl and 1 M NaCl aqueous electrolytes. It was seen that the CV profiles for 1 M LiCl and 1 M NaCl are completely different from those in the $AlCl_3$ electrolyte (Figure 5.6a and 5.6b). This suggests that the CV peaks observed in $AlCl_3$, are may be due to interaction of Al^{3+} ion in VOH.

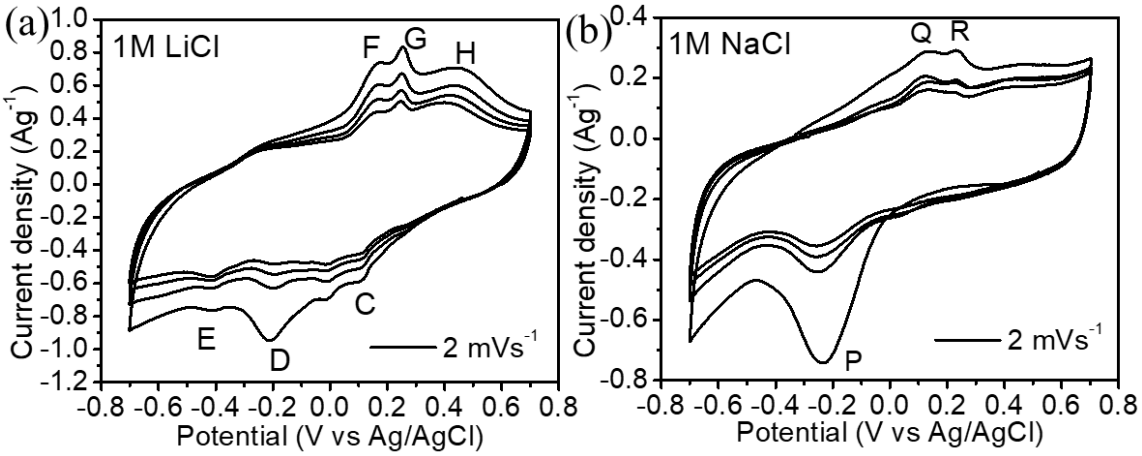

Figure 5.6: CV profiles of VOH in (a) 1 M LiCl and (b) 1 M NaCl aqueous electrolytes.

Moreover, the CV experiments of VOH were carried out in 1 M HCl and 0.5 M H_2SO_4 aqueous electrolytes at scan rate of 2 mVs^{-1} to observe the proton contribution. As displayed in Figure 5.7a and Figure 5.7b, the CV profiles differ when compared to those in $AlCl_3$ aqueous electrolyte, and the current response is significantly lower in both the 1 M HCl and 0.5 M H_2SO_4 aqueous electrolytes. This indicates negligible proton insertion in VOH.

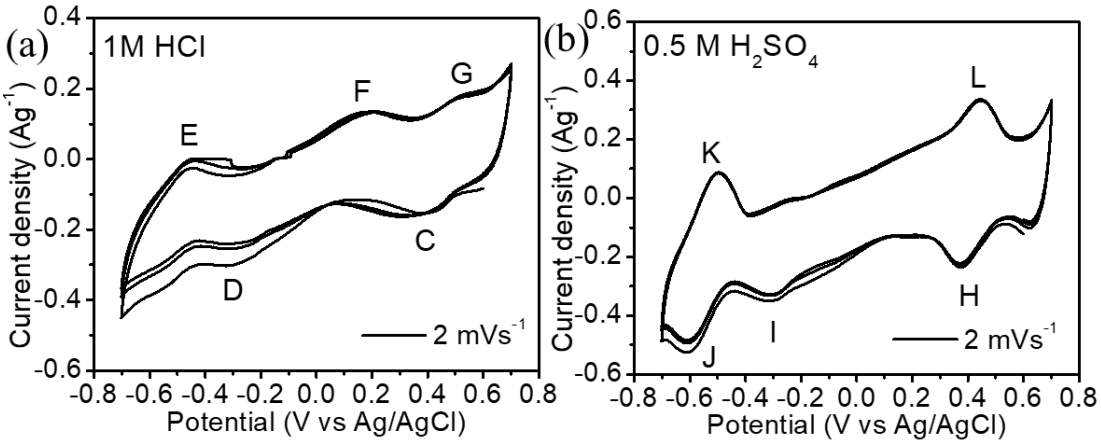

Figure 5.7: CV profiles of VOH in (a) 1 M HCl and (b) 0.5 M H_2SO_4 aqueous electrolytes.

Galvanostatic charge-discharge (GCD) experiments were performed for all the aqueous and gel electrolytes in the voltage range of -0.7 V to 0.7 V (Figure 5.8). The GCD profiles of VOH in all $AlCl_3$ aqueous and 1 M $AlCl_3$/PEO gel electrolytes are identical (Figure 5.8 (a-d)). The discharge/charge specific capacitance values for the first cycle at a current density of 1 Ag^{-1} were calculated as 345 Fg^{-1}/261 Fg^{-1}, 380 Fg^{-1}/208 Fg^{-1} and 434 Fg^{-1}/233 Fg^{-1} for the aqueous electrolytes 0.25 M $AlCl_3$, 0.5 M

$AlCl_3$ and 1 M $AlCl_3$ respectively (Figure 5.8 (a-c)). In contrast, the specific capacitance for the 1 M $AlCl_3$/PEO gel electrolyte is higher compared to the aqueous electrolytes. The first discharge/charge specific capacitance at the same current density (1 Ag^{-1}) was evaluated as 774 Fg^{-1}/392 Fg^{-1} (Figure 5.8d).

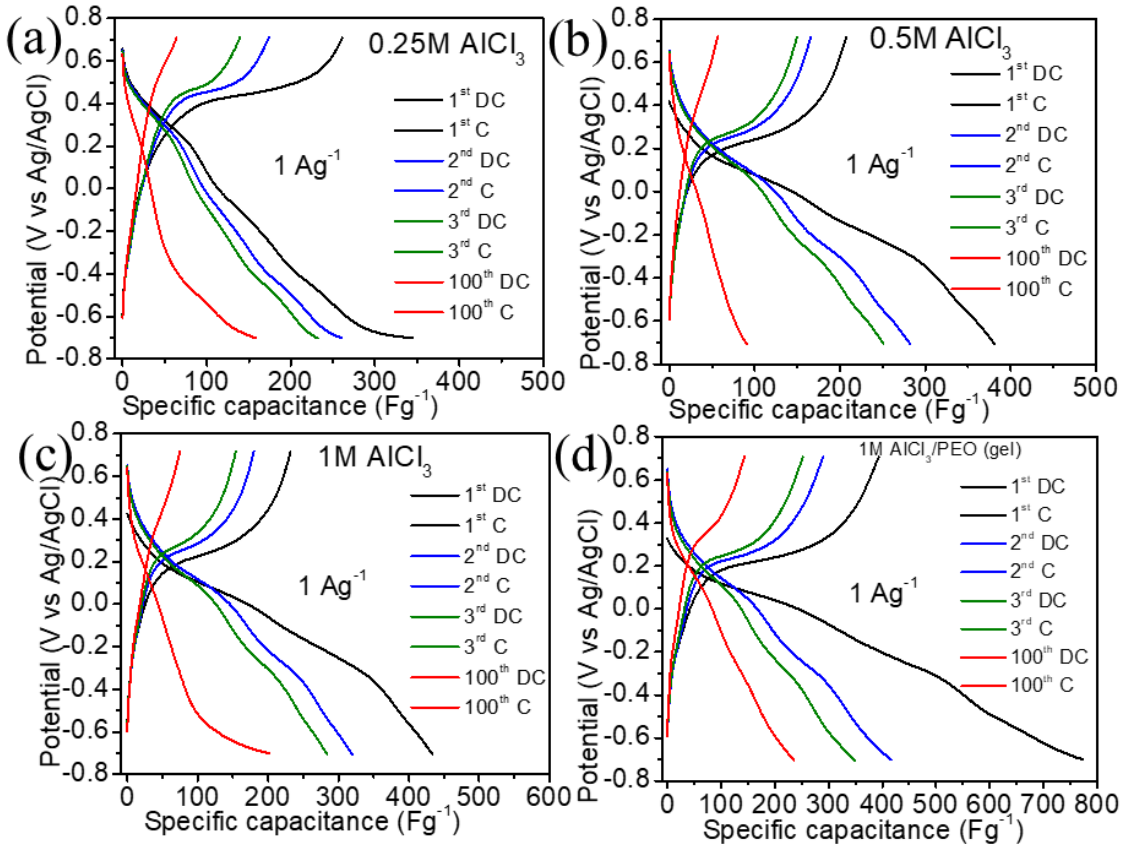

Figure 5.8: GCD profiles of VOH in (a) 0.25 M $AlCl_3$ (b) 0.5 M $AlCl_3$, (c) 1 M $AlCl_3$ aqueous electrolytes and (d) 1 M $AlCl_3$/PEO (gel) electrolytes.

Then, GCD experiments were conducted up to 100 cycles for all the aqueous and gel electrolytes (Figure 5.9). The specific capacitance values of VOH over 100 cycles at a current density of 1 Ag^{-1} were measured as 156 Fg^{-1}, 90 Fg^{-1}, 207 Fg^{-1}, and 235 Fg^{-1} for 0.25 M $AlCl_3$, 0.5 M $AlCl_3$, 1 M $AlCl_3$ aqueous, and 1 M $AlCl_3$/PEO gel electrolytes, respectively (Figure 5.9). Clearly, enhanced cycling stability was observed in the case of 1 M $AlCl_3$/PEO gel electrolyte.

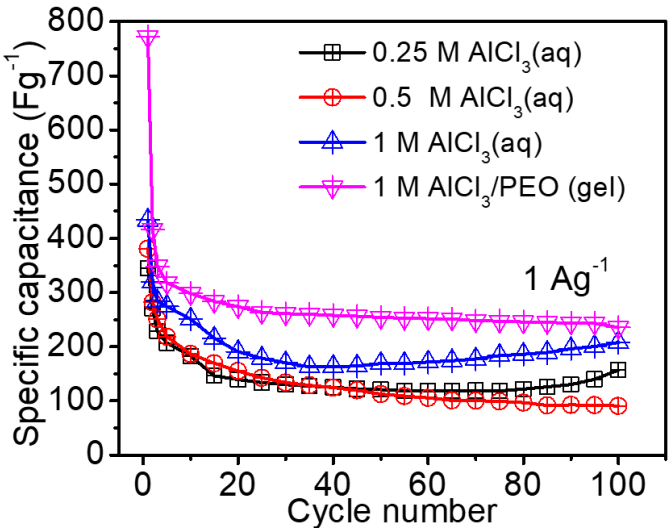

Figure 5.9: Specific capacitance versus cycle number at current density of 1 Ag^{-1} over 100 cycles for all the aqueous and gel electrolytes.

Electrochemical impedance spectroscopy (EIS) experiments were conducted for both the aqueous and gel electrolytes in the frequency range of 100 mHz to 100 kHz. Figure 5.10 presents the Nyquist plot of VOH in 1 M $AlCl_3$ aqueous and 1 M $AlCl_3$/PEO gel electrolytes, showing semicircles in the high frequency region and straight lines in the low frequency region. The intercepts on the X-axis represents the equivalent series resistance (ESR), which is the combination of intrinsic resistance of VOH and the ionic resistance of the electrolyte. The equivalent circuit diagram is highlighted in the inset of Figure 5.10. It was found that VOH electrode exhibits a lower (ESR) value (6.115 ohm) in the 1 M $AlCl_3$/PEO gel electrolyte compared to the ESR value (7.057 ohm) in the 1 M $AlCl_3$ aqueous electrolyte.

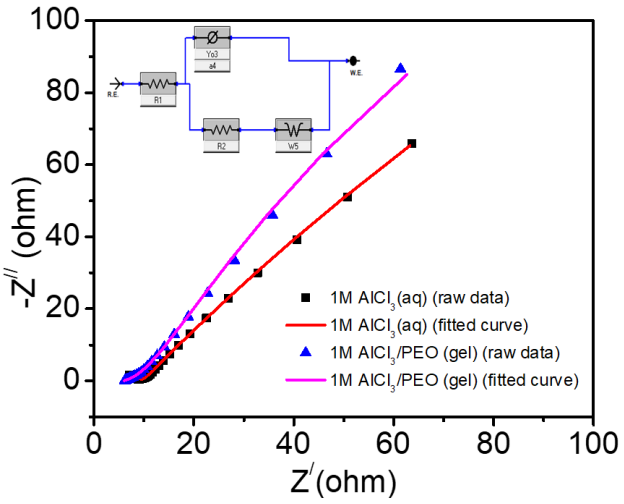

Figure 5.10: Nyquist plots of VOH electrode in 1 M $AlCl_3$ aqueous and 1 M $AlCl_3$/PEO gel electrolytes with the equivalent circuit diagram.

Apart from that, galvanostatic charge-discharge experiments were also conducted for 0.5 M $Al_2(SO_4)_3$ and 1 M $Al(NO_3)_3$ electrolytes at current density of 1 Ag^{-1}. It was observed that VOH shows contribution in both the electrolytes but the cycling stabilities were much lower compared to the 1 M $AlCl_3$ aqueous electrolyte (Figure5.11(a-c)).

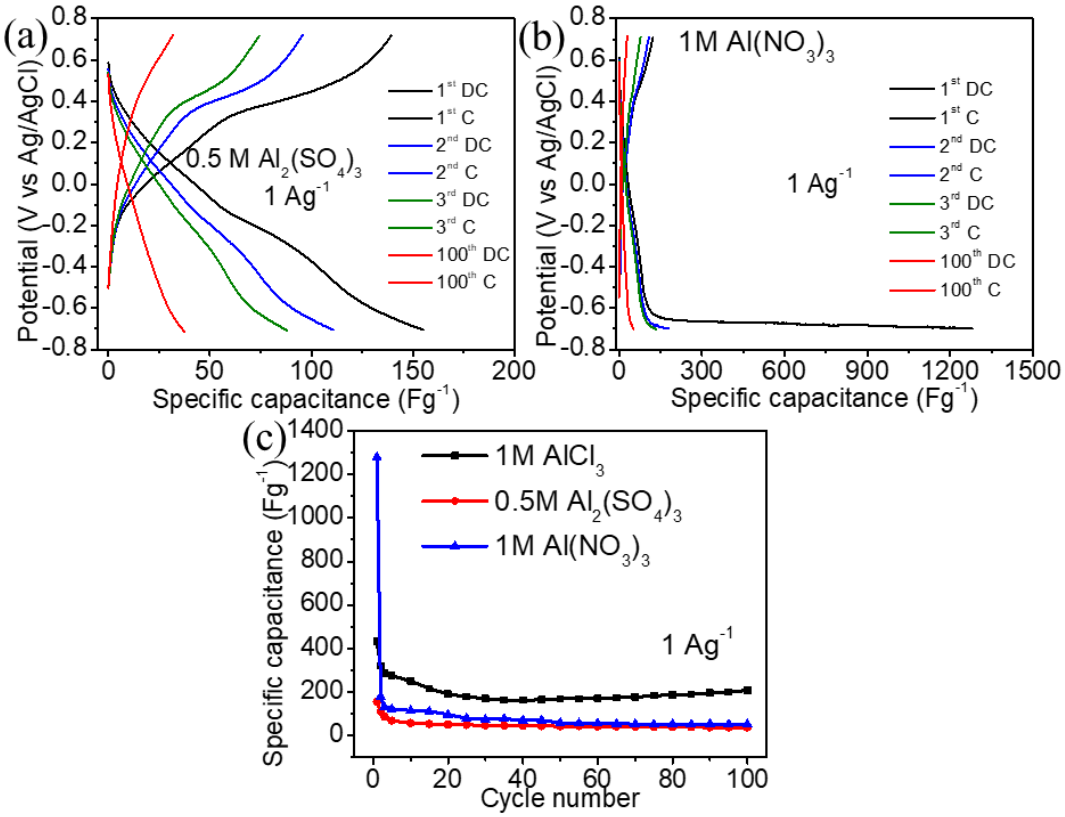

Figure 5.11: GCD profiles of VOH in (a) 0.5 M $AlCl_3$, (b) 1 M $Al(NO_3)_3$ at current density of 1 Ag^{-1} and (c) Specific capacitance versus cycle number.

Now, to investigate the ions kinetics, a series of CV experiments were performed at different scan rates ranging from 3 mVs^{-1} to 10 mVs^{-1} in 1 M $AlCl_3$ aqueous electrolyte (Figure 5.12a). The ion storage mechanism was analyzed using the power law equation $i = a\vartheta^b$, where a and b are tunable constants [18]. In general, b = 0.5 represents the diffusion control process, while b = 1 refers to a capacitive control process. As shown in the Figure 5.12b, the b values corresponding to the peaks A, A/, B and B/ were determined to be 0.55, 0.41, 0.50 and 0.73 respectively. These indicate that the electrochemical charge storage process is dominated by both diffusion process and surface absorption process [18]. Further, the total capacitance, which combines capacitive and diffusion responses was evaluated using the equation $i = k_1\vartheta + k_2\vartheta^{1/2}$ (where the terms $k_1\vartheta$ and $k_2\vartheta^{1/2}$ represent the surface capacitive and

diffusion control process respectively) [18]. Additionally, it was estimated that the capacitive contribution was about 65.4 % of the total capacitance at scan rate of 3 mVs^{-1}, which increased significantly to 77.6 % at higher scan rate of 10 mVs^{-1} (Figure 5.12c).

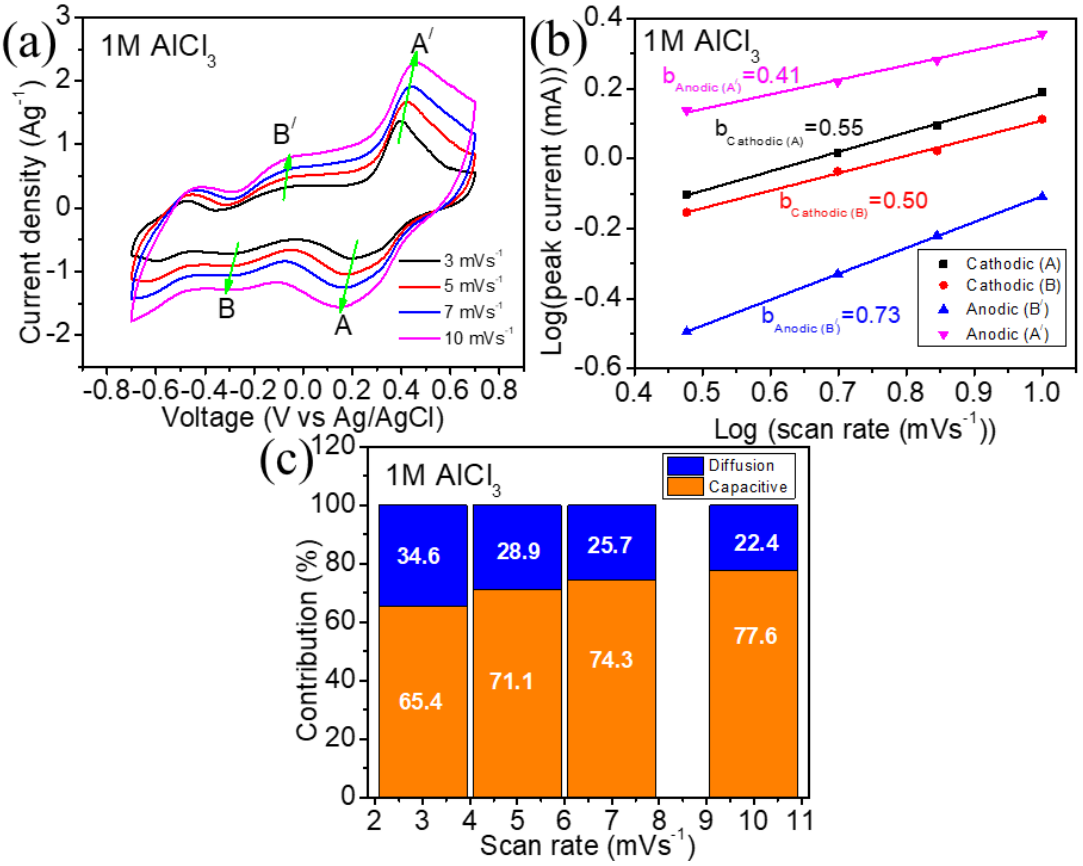

Figure 5.12: (a) CV profiles of VOH at scan rate from 3 mVs^{-1} to 10 mVs^{-1} in 1 M $AlCl_3$ aqueous electrolyte, (b) log (scan rate) vs log (peak current) plot and (c) charge storage contribution plot.

Again, electrochemical investigations were carried out in aluminium doped hydrated vanadate (AlVOH). For that, the crystal structure of the prepared AlVOH was confirmed by X ray diffraction. Figure 5.13a shows the XRD pattern of AlVOH, which clearly reveals the monoclinic structure with space group C2/m as indicated by JCPDS card no: 47-0146. In the Raman spectrum of AlVOH, all the characteristic peaks were slightly shifted, which may be presence of Al-O bond recognized at 658 cm^{-1} (Figure 5.13b). Similarly, in FTIR analysis, a small intensity additional peak was observed at 1401 cm^{-1} corresponding to the vibration of Al-O bond (Figure 5.13c). For surface morphology, FESEM images of AlVOH show the formation of microsphere with diameters ranging from ~ 7 μm to 10 μm (Figure 5.14 (a-b)).

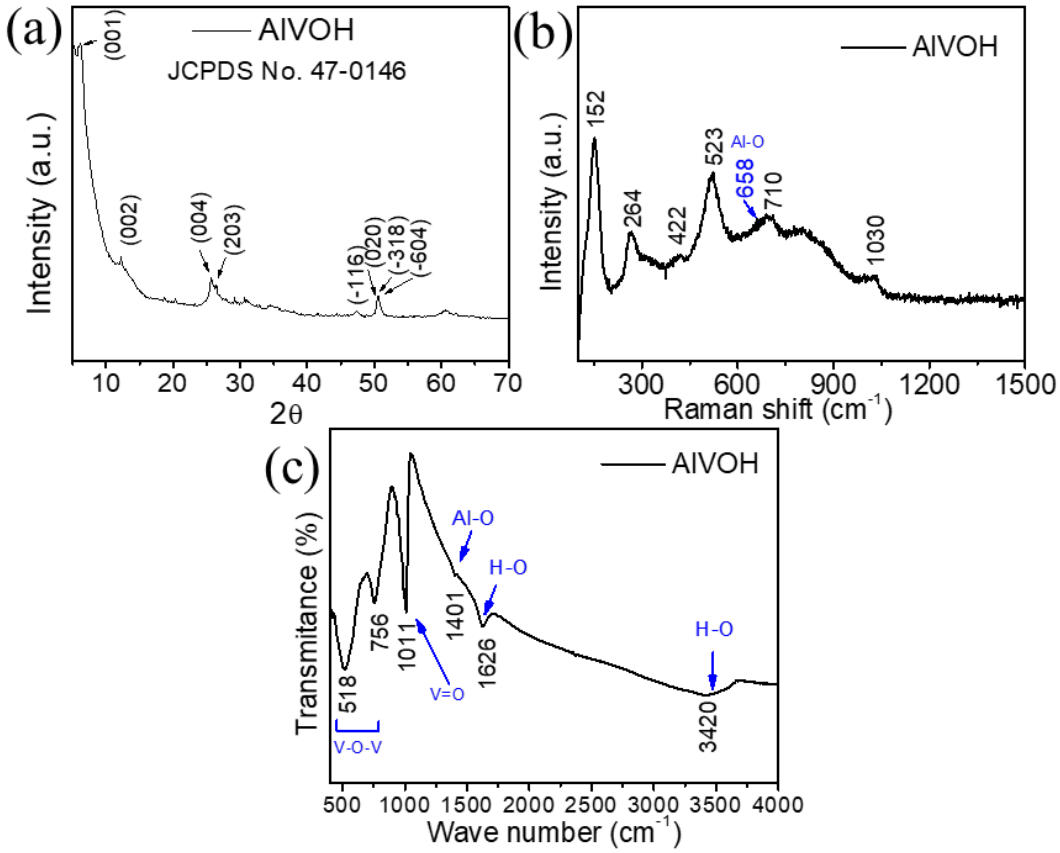

Figure 5.13: (a) XRD pattern, (b) Raman and (c) FTIR of AlVOH.

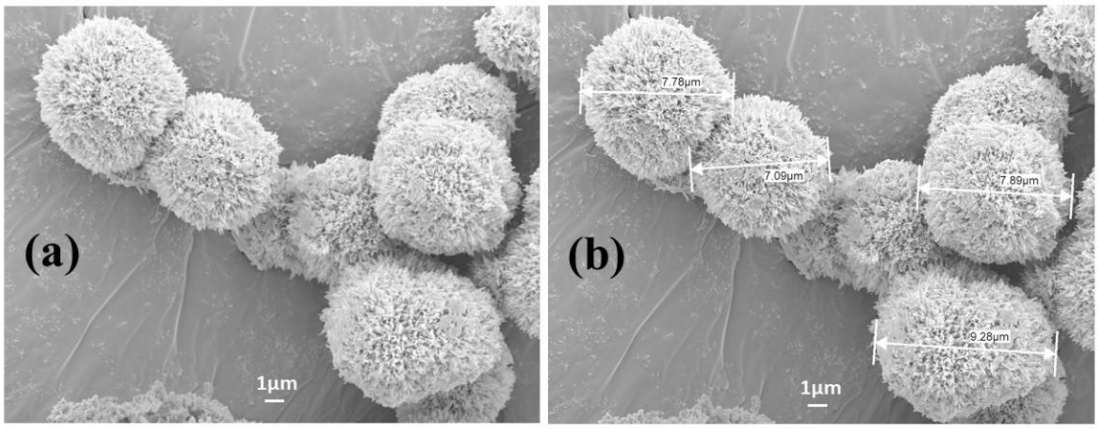

Figure 5.14: (a-b) FESEM images of AlVOH.

For the electrochemical investigation, CV experiments were performed on the AlVOH electrode in the potential window of -0.7 V to 7 V (vs Ag/AgCl) at a scan rate of 2 mVs^{-1} in 1 M $AlCl_3$, 0.5 M $Al_2(SO_4)_3$ and 1 M $Al(NO_3)_3$ aqueous electrolytes. As shown in Figure 5.15a, a pair of redox peaks (denoted as A/A$^{/}$) was observed at 0.10 V/0.35 V. Similar CV behaviors were noticed for 0.5 M $Al_2(SO_4)_3$ and 1 M $Al(NO_3)_3$ electrolytes. However, the identified redox peaks (B/B$^{/}$) and (C/C$^{/}$) were marked at 0.04 V/0.39 V and 0.10 V/0.39 V for 0.5 M $Al_2(SO_4)_3$ and 1 M $Al(NO_3)_3$ electrolytes

respectively (Figure 5.15b and 5.15c). It was noted that the current response sharply decreased in the lower potential side for the 1 M $Al(NO_3)_3$ electrolyte (Figure 5.15c).

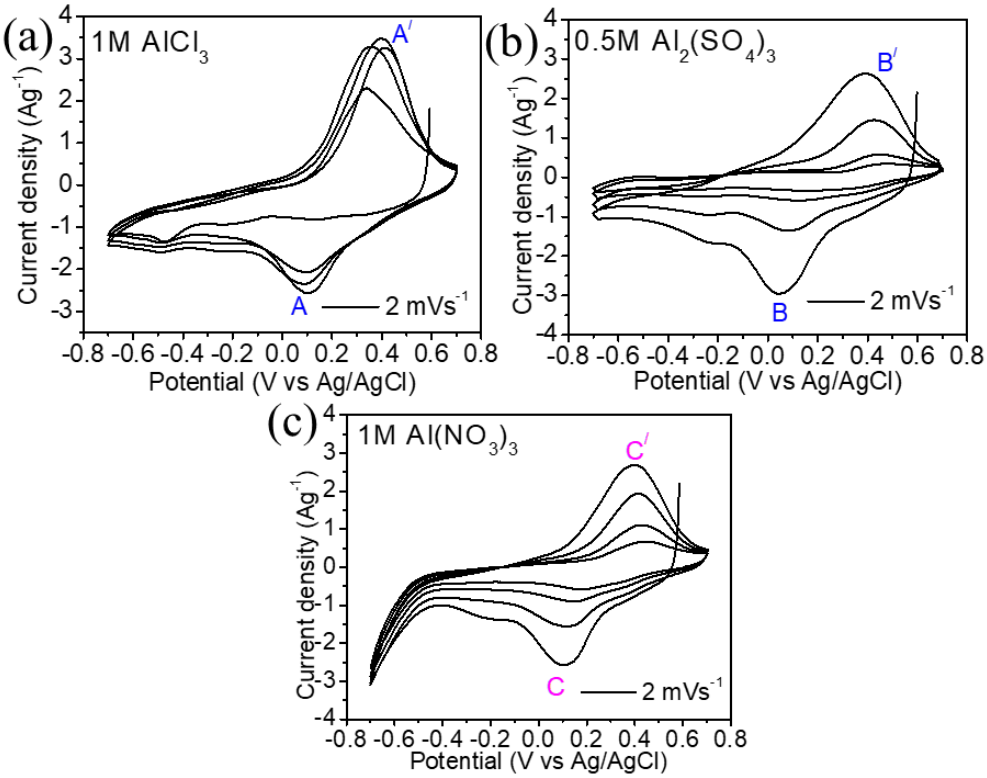

Figure 5.15: CV profiles of AlVOH in (a) 1 M $AlCl_3$, (b) 0.5 M $Al_2(SO_4)_3$ and (c) 1 M $Al(NO_3)_3$ aqueous electrolytes.

Galvanostatic charge-discharge experiments for AlVOH electrode were conducted in the identical potential window (i.e. -0.7 V to 0.7 V) (vs Ag/AgCl) at a current density of 1 Ag^{-1}.The discharge/charge specific capacitance values in the 1 M $AlCl_3$, 0.5 M $Al_2(SO_4)_3$ and 1 M $Al(NO_3)_3$ aqueous electrolytes were evaluated as 410 Fg^{-1}/200 Fg^{-1}, 280 Fg^{-1}/19 Fg^{-1} and 687 Fg^{-1}/234 Fg^{-1} respectively (Figure 5.16 (a-c)). Cycling stability experiments were then performed and the discharge specific capacitance values of the AlVOH electrodes at current density (= 1 Ag^{-1}) over 100 cycles were obtained as 68 Fg^{-1}, 48 Fg^{-1} and 54 Fg^{-1} in the 1 M $AlCl_3$, 0.5 M $Al_2(SO_4)_3$ and 1 M $Al(NO_3)_3$ aqueous electrolytes respectively (Figure 5.17). However, when compared the same to pure VOH, it was observed that pure VOH exhibited better stability in 1 M $AlCl_3$ aqueous electrolyte than AlVOH (Figure 5.17).

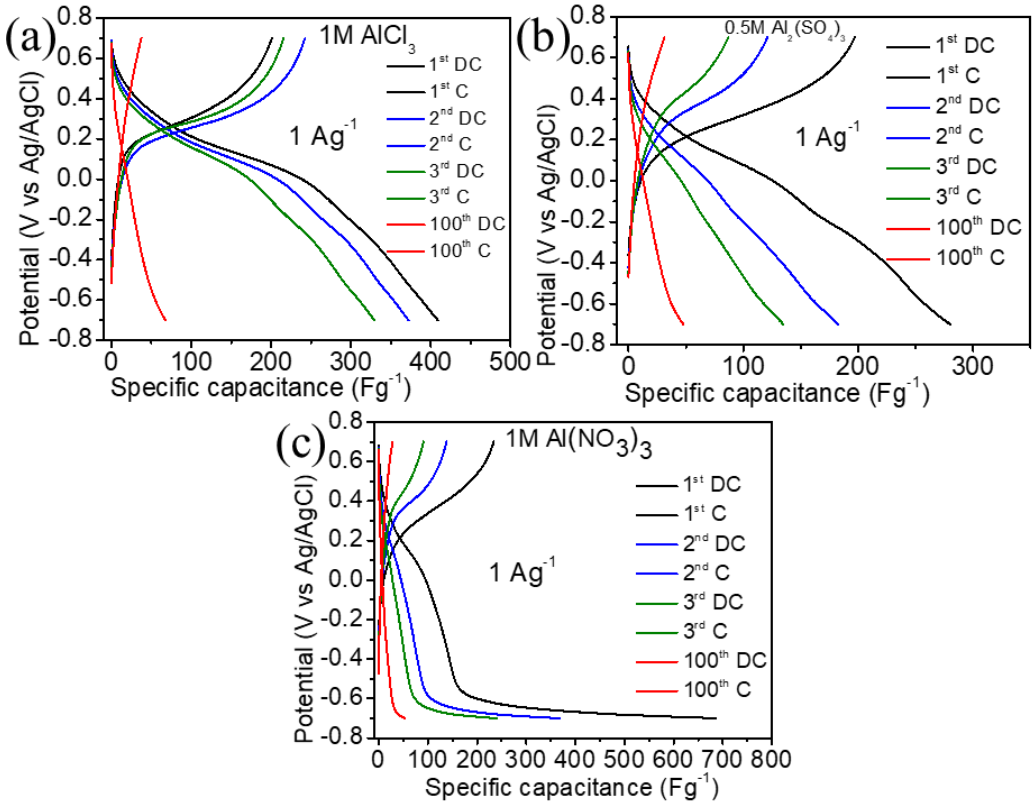

Figure 5.16: GCD profiles of AlVOH in (a) 1 M $AlCl_3$, (b) 0.5 M $Al_2(SO_4)_3$ and (c) 1 M $Al(NO_3)_3$ aqueous electrolytes.

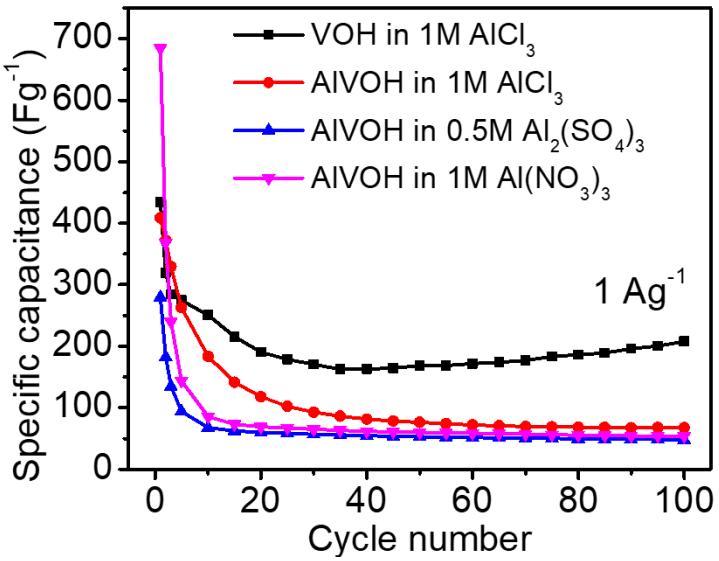

Figure 5.17: Comparison of cycling stability up to 100 cycles at current density of 1 Ag^{-1}.

Additionally, the experiments were carried out in 1 M $AlCl_3$/PEO gel electrolyte. Figure 5.18a, shows the CV curves of AlVOH in the same potential window (vs Ag/AgCl) at scan rate of 2 mVs^{-1}, which displayed a similar pattern. The redox peaks (denoted as E/E/) were noticed at 0.05 V/0.46 V. The discharge/charge specific capacitances at a current density of 1 Ag^{-1} were evaluated as 452 Fg^{-1}/425 Fg^{-1} (Figure 5.18b). Now, for the cycling stability test, GCD experiments were performed up to 100 Cycles. The specific capacitance of AlVOH at current density of 1 Ag^{-1} over 100 cycles in 1 M $AlCl_3$/PEO gel electrolyte was found to be 98 Fg^{-1}, which was higher than that in 1 M $AlCl_3$ aqueous electrolyte (Figure 5.18c). Then, comparing these values with pure VOH, revealed that pure VOH exhibited better cycling stability in the 1 M $AlCl_3$/PEO gel electrolyte (Figure 5.18c).

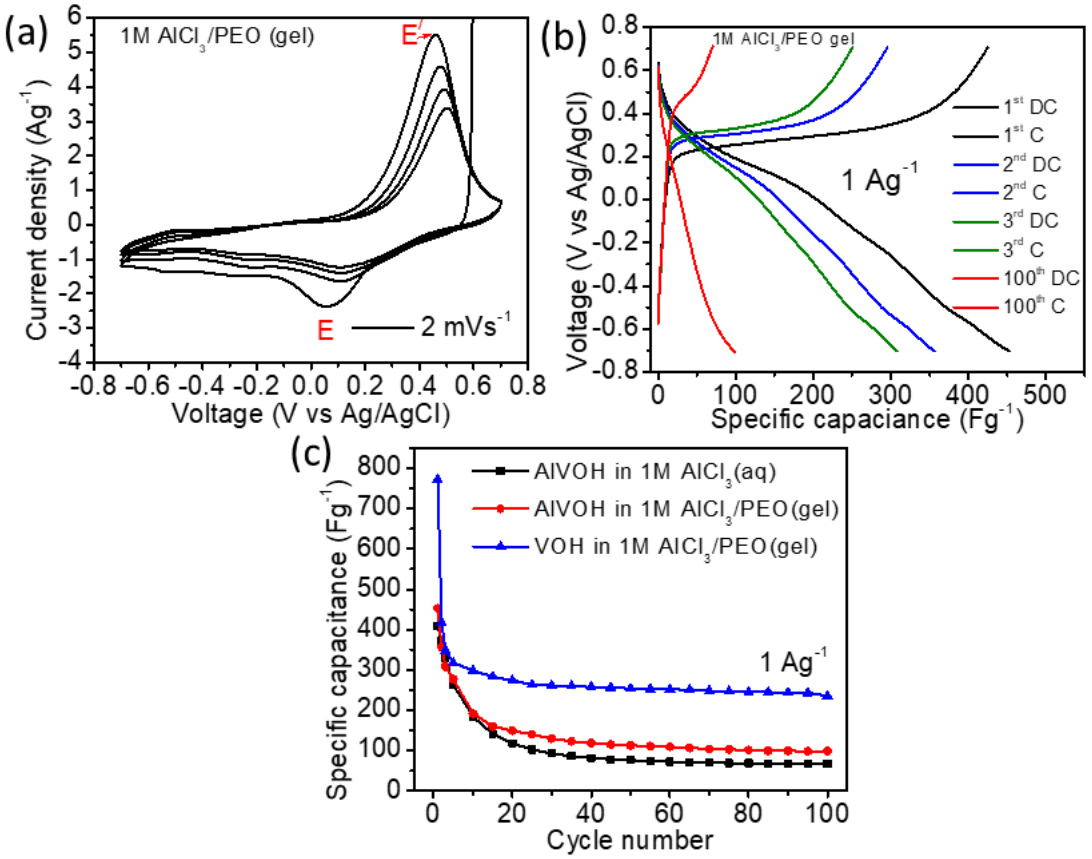

Figure 5.18: (a) CV profiles and (b) GCD profiles of AlVOH in 1 M $AlCl_3$/PEO gel electrolyte and (c) the comparison of cycling stability up to 100 cycles.

5.4 Conclusion

In this chapter, it was discussed that hydrated vanadate (VOH) was synthesized using hydrothermal method and investigated the Al^{3+} ion storage behavior

in various Al -ion based aqueous and gel electrolytes. It was observed that the charge storage kinetic in VOH is mostly governed by capacitive process. The cycling stability of VOH was enhanced, with a specific capacitance of up to 235 Fg^{-1} in the 1 M $AlCl_3$/PEO gel electrolyte, compared to only 156 Fg^{-1} in the 1 M $AlCl_3$ aqueous electrolyte. It was observed that pure VOH exhibited better cycling stability than AlVOH in both 1 M $AlCl_3$ aqueous and 1 M $AlCl_3$/PEO gel electrolytes.

5.4 References

[1] Gamal, H., Elshahawy, A. M., Medany, S. S., Hefnawy, M. A., and Shalaby, M. S. Recent advances of vanadium oxides and their derivatives in supercapacitor applications: A comprehensive review. *J. Energy storage,* 76: 109788, 2024.

[2] Yan, Y., Li, B., Guo, W., Pang, H., and Xue, H. Vanadium based materials as electrode materials for high performance supercapacitors. *J. Power Sources,* 329: 148-169, 2016.

[3] Saravanakumar, B., Purushothaman, K. K., and Muralidharan, G. High performance supercapacitor based on carbon coated V_2O_5 nanorods. *J. Electroanal. Chem.,* 758: 111-116, 2015.

[4] Wachs, I. E. Catalysis science of supported vanadium oxide catalysts. *Dalton Trans.,* 42: 11762-11769, 2013.

[5] Koohestani, B., Ahmad, A. L., Bhatia, S., and Ooi, B. S. Vanadium oxide based composite catalysts for the oxidation of styrene: A comparative study. *Current Nanoscience*, 7: 781-789, 2011.

[6] Kiran, P., Jasrotia, P., Verma, A., Kumar, A., Hmar, J. J. L., Jyoti., and Kumar, T. Vanadium pentoxide gas sensors: An overview of elemental doping strategies and their effect on sensing performance. *Catalysis Commun*., 187: 106838, 2024.

[7] Liang, F., Zheng, R., Long, F., Zhang, S., Zhong, S., Jia, S., Nong, J., Wang, Y., and Song, L. Vanadium oxide-based battery materials. https://doi.org/10.1007/s11581-024-05751-7

[8] Liu, P., Wang, B., Sun, X. M., Gentle, I., and Zhao, X. S. A comparative study of V_2O_5 modified with multi-walled carbon nanotubes and poly(3,4-ethylenedioxythiophene) for lithium-ion batteries. *Electrochim. Acta,* 213: 557, 2016.

[9] Wang, P., Zhang, y., Feng, Z., Liu, Y., and Meng, C. A dual polymer strategy boosts hydrated vanadium oxide for ammonium-ion storage. *J. Colloid and Interface Science*, 606: 1322-1332, 2022.

[10] Lee, H. Y., and Goodenough, J. B. Ideal supercapacitor behavior of amorphous V_2O_5. nH_2O in potassium chloride (KCl) aqueous solution. *J. Solid State Chemistry*, 148: 81-84, 1999.

[11] Fan, Y., Yu, Y., Wang, P., Sun, J., Hu, M., Sun, J., Zhang, Y., and Huang, C. Free standing vanadium oxide hydration/reduced graphene oxide film for ammonium ion supercapacitors. *J. Colloid and Interface Science*, 633: 333-343, 2023.

[12] Xu, J., Zhang, Y., Liu, C., Cheng, H., Cai, X., Jia, D., and Lin, H. Al^{3+} Introduction hydrated vanadium oxide induced high performance for aqueous zinc ion batteries. *Small*, 18: 2204180, 2022.

[13] Du, Y., Zhang, Y., Wang, X., and Sun, J. Mg^{2+} pre intercalated hydrated vanadium oxide as high-performance cathode for aqueous zinc-ion batteries. *Modern Physics Letters B*, 36: 2242023, 2022.

[14] Zheng, J., Liu, C., Tian, M., Jia, X., Jahram, E. P., Seidler, G. T., Zhang, S., Liu, Y., Zhang, Y., Meng, C., and Cao, G. Fast and reversible zinc ion intercalation in Al-ion modified hydrated vanadate. *Nano energy*, 70: 104519, 2020.

[15] Liu, C., Neale, Z., Zheng, J., Jia, X., Huang, J., Yan, M., Tian, M., Wang, M., Yang, J., and Cao, G. Expanded hydrated vanadate for high performance aqueous zinc ion batteries. *Energy Environ. Sci*. 12: 2273-2285, 2019.

[16] Nandi, S., Yan, Y., Yuan, X., Wang, C., He, X., Li, Y., and Das, S. K. Vanadyl ethylene glycolate: A novel organic-inorganic electrode material for rechargeable aqueous aluminum-ion battery. *Solid State Ionics*, 389: 116085, 2023.

[17] Kalita, M. P. C., Sarma, S., and Borah, P. Effects of Co and Mn doping on structural, optical and magnetic properties of hydrated vanadium pentoxide (V_2O_5.nH_2O) nanocrystals. *Brazilian Journal of Physics*, 52: 195, 2022.

[18] Wen, N., Chen, S., Li, X., Zhang, K., Feng, J., Zhou, Z., Fan, Q., Kuang, Q., Dong, Y., and Zhao, Y. Facile synthesis of one dimensional vanadyl acetate nanobelts toward a novel anode for lithium storage. *Delton Trans*., 50: 11568, 2021.